

pubs.acs.org/JPCL Letter

X-ray/Extreme Ultraviolet Floquet State Multidimensional Spectroscopy, an Analogue of Multiple Quantum Nuclear Magnetic Resonance

John C. Wright,* Daniel D. Kohler, and Uwe Bergmann

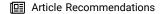


Cite This: J. Phys. Chem. Lett. 2023, 14, 4908–4913



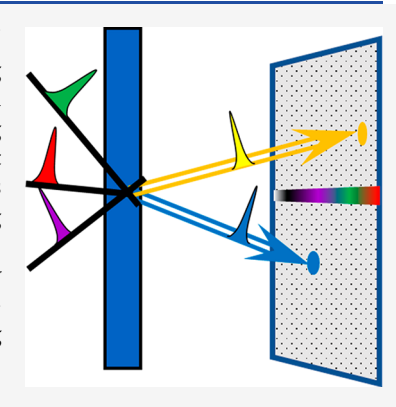
ACCESS I

III Metrics & More



Supporting Information

ABSTRACT: There is great interest in developing fully coherent multidimensional X-ray/extreme ultraviolet (XUV) spectroscopic techniques because of their capability for achieving atomic spectral selectivity. Current proposals rest on using sequentially and coherently driven core excitations with multiple X-ray/XUV excitation pulses and measuring the output using time domain Fourier transform methods. In this paper, we propose an alternative method that creates an entanglement of core and optical transitions to form a Floquet state that creates directional and coherent output beams. Multidimensional spectra are obtained by measuring the intensity of output beams while tuning the optical frequencies across resonances. This approach expands on previous optical pump—XUV probe spectroscopy of MoTe₂ by theoretically demonstrating its multidimensional capabilities. Both parametric and non-parametric pathways are proposed to optimize the resolution of inhomogeneous broadening and k-selective features.



he invention of the laser brought with it the promise of creating an optical analogue of multidimensional nuclear magnetic resonance (NMR). The search divided in two directions¹ that differed in whether multiple quantum states are simultaneously and periodically driven by strong fields to create Floquet states^{2,3} or sequentially driven to resolve the phase oscillations of individual coherences.⁴ There is now interest in developing X-ray and extreme ultraviolet (XUV) analogues that provide coherent multidimensional spectra (CMDS) and atomic level resolution of molecular and material systems. 5-7 Current proposals are based on sequentially and coherently driving individual valence core coherences with Xray or XUV pulses.⁶ These proposals are difficult to experimentally implement because of the need for interferometric phase stability between attosecond XUV/X-ray pulses. Recent publications developed an alternative optical pump-XUV probe spectroscopy that is directly relevant to the work presented here. In the first, the optical excitation of an exciton in a MoTe2 thin film was used to create an electron/hole pair that resulted in new core electron transitions that fill the valence band hole and a Pauli blocking of the excitation to the populated conduction band state.9 The XUV and optical excitations were k-selective; therefore, it became possible to resolve the frequency changes resulting from hot carriercarrier thermalization, cooling, and recombination dynamics. There are also transient grating experiments that combine two angled optical pulses to create a transient grating and an XUV pulse to probe the subsequent dynamics.^{7,10,11} Because the process was fully coherent, phase matching could be used to

resolve the angles, frequencies, and relaxation rates of the different coherent output beams.

In this paper, we explore the feasibility of extending the previous optical pump-XUV probe work on MoTe₂ thin films⁹ to a non-perturbative scheme based on Floquet states that entangle mixtures of valence-to-core, excited electronic, and/or vibrational states, $\Psi_{\text{Floquet}} = \sum_{n} c_n \psi_n$. This approach builds on the success of a new family of frequency-domain CMDS methods that entangle electronic and/or vibrational states.3,12,13 Including core state excitation in the Floquet state will give both atomic and chemical bonding resolution capabilities. Figure 1a represents an experimental implementation of X-ray/XUV optical Floquet state spectroscopy using frequencies and pulse widths representative of the previous optical pump-XUV probe experiment. Three temporally and spatially overlapping excitation fields, $E = \sum_{i=1}^{3} E_i^0 \exp[i(\vec{k}_i \vec{z} - \omega_i t)]$, are focused into a sample at angles where they excite transitions from the v_{-n} core and v_0 upper valence band states. The ω_1 and ω_2 beams are spectrally narrow and continuously tunable over visible and ultraviolet. The ω_3 beam is a broadband XUV or X-ray beam. New beams

Received: March 22, 2023 Accepted: May 15, 2023



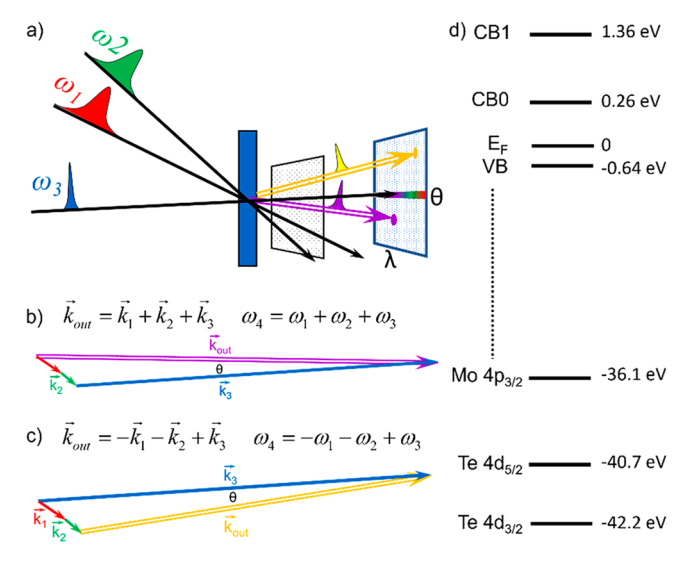


Figure 1. (a) Focusing three excitation pulses into a sample creates multiple output beams. A diffraction grating disperses the frequencies onto an array detector in the horizontal direction, and the phase matching changes the beam angles in the vertical dimension. (b and c) Phase matching of the k vectors defines the directionality of the output beams for two different output frequencies. (d) Energy levels of valence band core states and two of the conduction band states relative to the Fermi level.

are emitted from the output coherences in directions and frequencies defined by phase matching and energy conservation. Figure 1b shows two examples of phase matching at angles defined by $k_4 = k_1 + k_2 + k_3$ or $k_4 = -k_1 - k_2 + k_3$ and frequencies defined by $\omega_4 = \omega_1 + \omega_2 + \omega_3$ or $\omega_4 = -\omega_1 - \omega_2 + \omega_3$ ω_3 , respectively. After passing through a monochromator, the output beams are measured by an array detector that resolves the angular directions and frequencies of the emitted beams. The broad XUV excitation pulse appears at $\theta = 0$ mrad on the y axis of the array detector and across its range of wavelengths on the x axis. It serves as the probe in previous pump-probe experiments. The fully resonant output beams appear at $\theta > 0$ and θ < 0 mrad for the parametric and non-parametric pathways, respectively. Scanning the optical excitation frequencies creates multidimensional spectra from the multiplicative resonance enhancements that will be both atomically selective and k-vector-selective within the Brillouin zone. Figure 1d shows a sketch of the core, valence band, and conduction band states at the k point in the Brillouin zone for MoTe₂.

Figure 2 shows the wave mixing energy level (WMEL) and Liouville diagrams¹⁴ for the optical pump-XUV probe spectroscopy experiments described above. The WMEL diagram defines the transitions, and the Liouville diagram defines the coherence pathways between filled valence states and two conduction band states. The energy states are labeled by the transitions that occur from a core state (labeled v_{-n}) and the band edge valence band state (v_0) to higher excited states $(e_0 \text{ and/or } e_1)$. The two labels to the far left define the core and valence band states involved in these transitions. The energy level diagram differs from that of Figure 1d. In this diagram, the bottom level represents the ground state and the others are excited levels. For example, the pump transitions excite an excitonic population in the e_0 state, leaving a hole in the band edge valence state, v_0 . The XUV probe excites a transition from a core state to the empty hole in v_0 , leaving a core state hole.

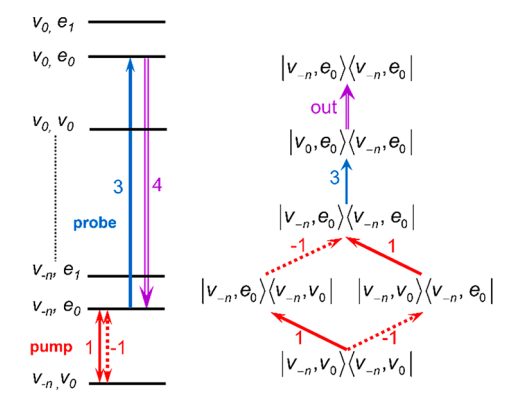


Figure 2. WMEL and Liouville diagrams for an optical pump—XUV probe experiment. The solid and dotted arrows define the time ordering (from left to right) of the ket and bra interactions that create the series of populations and coherences.

The third transition transfers the ν_0 hole to the ν_{-n} core state, resulting in a bleach of the XUV probe. The Liouville diagram shows the two time-ordered ket and bra pathways, $|i, m\rangle\langle j, n|$.

The proposed optical, XUV Floquet state spectroscopy technique uses the same transitions as the optical pump-XUV probe, but it is fully coherent. The temporally overlapped excitation pulses entangle the core, valence, and conduction band states; therefore, they strongly perturb each other, i.e., shakeup interactions. Figure 3 shows the WMEL and Liouville diagrams for the proposed fully coherent threewave mixing (panels a and b of Figure 3) and four-wave mixing (panels c and d of Figure 3) pathways. 14 The parametric pathways (panels a and c of Figure 3) do not deposit energy in the system, while non-parametric pathways (panels b and d of Figure 3) do. 13 The pathways differ in many ways that make them complementary to each other (vide infra). Because threewave mixing pathways require a loss of inversion symmetry, they selectively resolve molecules at interfaces. The four-wave mixing pathways do not require symmetry breaking. They also differ in their ability to resolve inhomogeneous broadening and individual states within the Brillouin zone.16

The transitions that create a Floquet state have a single time ordering because the core level transition to the valence band edge requires a hole created by a prior optical transition from the valence band edge to the conduction band. The solid and dotted arrows show the ket and bra transitions responsible for the three-wave mixing parametric $(|v_0, e_0\rangle\langle v_{-n}, v_0|)$ and nonparametric $(|e_0, v_0\rangle\langle v_{-n}, e_0|)$ output coherences and the fourwave mixing parametric $|v_0, e_1\rangle\langle v_{-n}, v_0|$ and non-parametric $|e_1, v_0\rangle\langle v_{-n}, e_1|$ output coherences.

The energy dispersions of bands across the Brillouin zone reflect the details of crystal bonds and give rise to inhomogeneous broadening with either positive or negative correlations. The parametric and non-parametric pathways have coherent interference between fully resonant and partially resonant k points that yield different but complementary abilities to resolve these correlations. The coherence interference depends upon the relative signs of the real and imaginary components of the density matrices. The relative phases of the individual coherences are identical for each of the three resonances in the parametric pathway. For the non-parametric pathway, one of the resonances has the opposite relative phase from the others. These are the same factors that define whether a coherence pathway is rephasing or non-rephasing for time domain experiments. In frequency domain

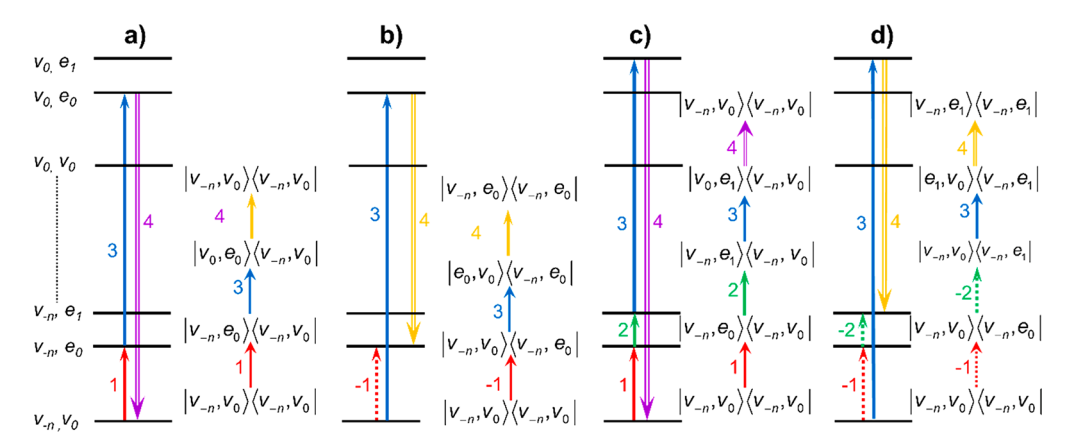


Figure 3. Time ordered transitions (from left to right) and sequence of coherences created by multiple excitation pulses. The last transition is the output signal. The two state notations on the left represent the states involving excitation of an electron from the v_{-n} core or an electron from the top of the valence band, v_0 . The coherence pathway shows the evolution of the $|i,j\rangle\langle m,n|$ ket and bra states. Panels a and c are parametric pathways, and panels b and c are non-parametric pathways. Panels a and b are three-wave mixing pathways, and panels c and d are four-wave mixing pathways.

experiments, if the frequencies are fully resonant with a specific member of the ensemble, the interference with the remaining members of the ensemble will be either constructive or destructive. If it is destructive, the larger, partially resonant contribution will cancel that of the fully resonant part of the ensemble and correlations of the band dispersions will not be resolved. If it is constructive, the partially resonant contributions will further enhance the fully resonant member of the ensemble and the correlation of the band dispersions will be resolved. If the changes in the transition frequencies of the multiple resonances are correlated, the dispersion will be resolved in the non-parametric pathway and not in the parametric pathway. If they are anticorrelated, the resolving capabilities are the opposite.

The amplitude and spatial and temporal oscillations of the $|m\rangle\langle n|$ coherences are defined by the density matrix elements, $\rho_{nm} \equiv \tilde{\rho}_{nm} \exp[i(\vec{k}_{nm}\vec{z} - \omega_{mn}t)]$, where $\rho_{nm} \equiv c_n c_m^*$. In the steady-state limit, the $\rho_{e_0\nu_{-n}}$ and $\rho_{\nu_0\nu_{-n}}$ density matrices of the $|\nu_0, e_0\rangle\langle \nu_{-n}, \nu_0|$ and $|e_0, \nu_0\rangle\langle \nu_{-n}, e_0|$ output coherences in panels a and b of Figure 3 are

$$\begin{split} & \rho_{e_{0^{\nu}-n}} \equiv \frac{\Omega_{1}\Omega_{3}}{4\Delta_{e_{0^{\nu}_{0}}}\Delta_{e_{0^{\nu}-n}}} \rho_{\nu_{-n}\nu_{0};\nu_{-n}\nu_{0}} \quad \text{and} \\ & \rho_{\nu_{0^{\nu}-n}} \equiv -\frac{\Omega_{1}\Omega_{3}}{4\Delta_{\nu_{0}e_{0}}\Delta_{\nu_{0^{\nu}-n}}} \rho_{\nu_{-n}\nu_{0};\nu_{-n}\nu_{0}} \end{split} \tag{1}$$

where

$$\begin{split} & \Delta_{\epsilon_0 v_0} \equiv \omega_{\epsilon_0 v_0} - \omega_1 - i \Gamma_{\epsilon_0 v_0} \\ & \Delta_{v_0 \epsilon_0} \equiv \omega_{v_0 \epsilon_0} + \omega_1 - i \Gamma_{\epsilon_0 v_0} \\ & \Delta_{\epsilon_0 v_{-n}} \equiv \omega_{\epsilon_0 v_0} - \omega_1 - \omega_3 - i \Gamma_{\epsilon_0 v_{-n}} \\ & \Delta_{v_0 v_{-n}} \equiv \omega_{v_0 v_{-n}} + \omega_1 - \omega_3 - i \Gamma_{v_0 v_{-n}} \\ \end{split}$$

The $\rho_{e_1\nu_{-n}}$ and $\rho_{\nu_0\nu_{-n}}$ density matrices of the $|\nu_0, e_1\rangle\langle\nu_{-n}, \nu_0|$ and $|e_0, \nu_0\rangle\langle\nu_{-n}, e_1|$ output coherences in panels c and d of Figure 3 are

$$\begin{split} & \rho_{e_{1}\nu_{-n}} = \frac{\Omega_{1}\Omega_{2}\Omega_{3}}{8\Delta_{e_{0}\nu_{0}}\Delta_{e_{1}\nu_{0}}\Delta_{e_{1}\nu_{-n}}} \rho_{\nu_{-n}\nu_{0};\nu_{-n}\nu_{0}} \quad \text{and} \\ & \rho_{\nu_{0}\nu_{-n}} = \frac{\Omega_{1}\Omega_{2}\Omega_{3}}{8\Delta_{\nu_{0}e_{0}}\Delta_{\nu_{0}e_{1}}\Delta_{\nu_{0}\nu_{-n}}} \rho_{\nu_{-n}\nu_{0};\nu_{-n}\nu_{0}} \end{split} \tag{3}$$

, respectively. Here

$$\begin{split} \Delta_{\epsilon_0\nu_0} &\equiv \omega_{\epsilon_0\nu_0} - \omega_1 - i\Gamma_{\epsilon_0\nu_0} \\ \Delta_{\nu_0\epsilon_0} &\equiv \omega_{\nu_0\epsilon_0} + \omega_1 - i\Gamma_{\epsilon_0\nu_0} \\ \Delta_{\epsilon_1\nu_0} &\equiv \omega_{\epsilon_1\nu_0} - \omega_1 - \omega_2 - i\Gamma_{\epsilon_1\nu_0} \\ \Delta_{\nu_0\epsilon_1} &\equiv \omega_{\nu_0\epsilon_1} + \omega_1 + \omega_2 \\ &- i\Gamma_{\epsilon_1\nu_0} \\ \Delta_{\epsilon_1\nu_{-n}} &\equiv \omega_{\epsilon_1\nu_{-n}} - \omega_1 - \omega_2 - \omega_3 - i\Gamma_{\epsilon_1\nu_{-n}} \\ \Delta_{\nu_0\nu_{-n}} &\equiv \omega_{\nu_0\nu_{-n}} - \omega_3 + \omega_1 \\ &+ \omega_2 - i\Gamma_{\nu_0\nu_{-n}} \end{split}$$

and $\omega_{nm} \equiv \omega_n - \omega_m$, $\Omega_i \equiv \frac{\mu_{nm} E_i}{\hbar}$, Γ_{nm} are the coherence frequency, Rabi frequency, and dephasing rate of the nm coherence, respectively, and ω_i is the frequency of the i excitation field.

The nonlinear polarization created by the output coherence is given by

$$P_{\rm NL}^{\rm o} = 2NF\mu_{\rm out}\tilde{\rho}_{\rm out} \tag{5}$$

where N and F are the concentration and local field correction factor, respectively. The nonlinear polarization creates an output beam intensity given by

$$I_{\text{out}} = \frac{2\pi\omega_{\text{out}}^2 F_{\text{out}}^2 \mu_{\text{out}}^2 N^2 I^2}{n_{\text{out}}^2} |\rho_{\text{out}}|^2 \operatorname{sinc}^2 \frac{\Delta k I}{2}$$
 (6)

where $\Delta k = k_{\rm out} - k_4$ and l are the wavevector difference between the output beam and nonlinear polarization. Because the transition moments, concentration, and path length also determine the absorbance, A, this equation can be rewritten in a form that defines the ratio of the fully resonant XUV output intensity to the XUV excitation intensity.

$$\frac{I_{\text{out}}}{I_3} = \frac{A_3 A_4 \omega_{\text{out}} \Omega_1^2 \Omega_2^2}{64 n_3 n_{\text{out}} \omega_3 \Gamma_{\epsilon_0 \nu_0}^2 \Gamma_{\epsilon_1 \nu_0}^2} |\rho_{\nu_{-n} \nu_0; \nu_{-n} \nu_0}|^2 \operatorname{sinc}^2 \frac{\Delta k l}{2}$$
(7)

A detailed derivation appears in the Supporting Information.

Except for the ω_2 intraband transition in Figure 2, the other transitions are identical to those used for the MoTe₂ optical pump–XUV probe experiment; therefore, the parameter values from that experiment can be used to estimate the $I_{\rm out}/I_3$ ratio. Our values are only estimates because our treatment neglects the changes that a full Floquet treatment would require. In fact, these estimates might be substantially changed because of the coupling caused within the Floquet state from the coulombic interactions created by the presence of a core

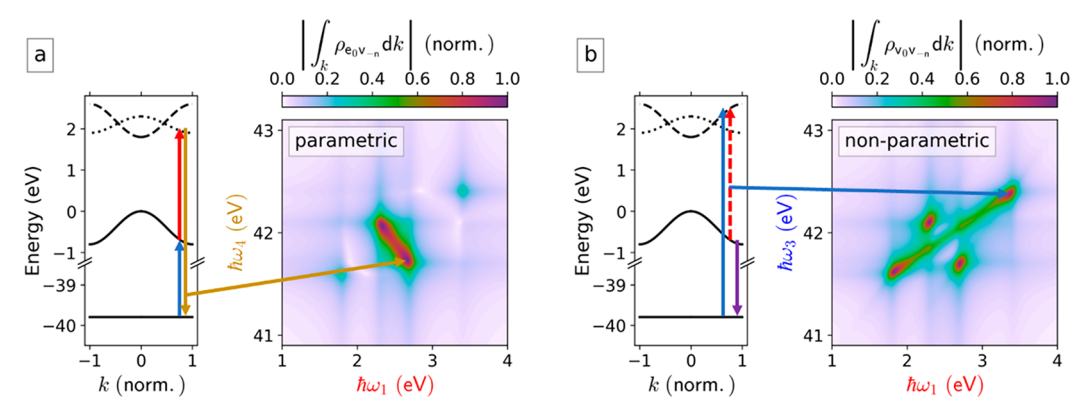


Figure 4. Examples of *k*-selective three-wave mixing Floquet state spectroscopy for the (a) parametric and (b) non-parametric pathways shown in panels a and b of Figure 3. They contain a simple model of a Brillouin zone with core, valence, and two conduction band states and the 2D spectra that result from scanning the frequencies of the two excitation beams. The colored arrows and axes labels correlate the transitions with their frequencies.

hole, i.e., shakeup effects. The presence of a core hole typically causes mixing between the equilibrium quantum states of $\sim 10\%$ and results in frequency shifts and the presence of dark states in a spectrum. ¹⁹

The Supporting Information and Table S1 summarize these values and the methods used to define them. The phase matching relations are also summarized in the table. Phase matching is possible for both the parametric and nonparametric pathways, but the angles required between the excitation beams are large. Because Δkl is small for the 50 nm thickness of a MoTe₂ sample, the phase matching angles are chosen to optimize the output intensity and the discrimination of the excitation and output beams. The Supporting Information contains details on this choice. The resulting estimate for the fully resonant I_{out}/I ratio is 1.3×10^{-3} , where Iis the XUV pulse intensity. This ratio is typical of similar CMDS methods.²⁰ High harmonic generation (HHG) XUV pulses have $\sim 10^7$ photons/pulse, while X-ray free-electron lasers have ~10¹²-10¹³ photons/pulse. A typical XUV pulse bandwidth is ~20 eV, while the multidimensional features have spectral widths determined by the dephasing rate of the valence band hole or conduction band electron, typically ~25 meV. If the fully resonant mixing efficiency is $I_{out}/I_3 = 1.3 \times I_{out}/I_3 = 1.$ 10^{-3} , where I_3 is the XUV pulse, there will be 16 photons/ pulse at the phase matched angle. For a 1 kHz pulse rate and 1 s measurement time, the output will be \sim 16,000 photons. The output and ω_3 beams will be spatially separated by the phasematching angle. The limit of detection will be determined by the discrimination between the broadband XUV excitation pulse occurring in the direction of the ω_3 beam and the nonresonant background occurring in the phase-matched direction of the ω_4 beam. The discrimination can be enhanced by increasing the phase-matching angle.

Figure 4 shows two two-dimensional (2D) *k*-selective Floquet spectra using the parametric and non-parametric pathways of panels a and b of Figure 3. The hypothetical band structure has two conduction bands, which contribute two different continua to the spectrum. Figure 4a shows the 2D spectrum for the parametric pathway. As discussed above, the parametric technique resolves the continuum correlation if the frequencies of both transitions are anti-correlated across *k* space. The dotted line conduction band exhibits this anti-correlation: increases in core excitation (blue arrow) frequency are matched by decreases in the optical excitation (red arrow)

frequency. As a result, the continuum is resolved as a bright antidiagonal line shape. Similarly, Figure 4b shows the 2D spectrum for the non-parametric pathway. This spectrum does not resolve the correlation of the dotted conduction band but instead resolves the correlated resonances with different k points of the dashed line conduction band. While parametric and non-parametric techniques exhibit different resolution of the continuum, the 2D resonances at band extrema are resolved in both techniques. The correlation type becomes less important at band extrema because the density of states is discontinuous and gives asymmetric interference.

The parametric and non-parametric processes described in this paper are specific examples for material spectroscopy, but there is a much broader set of pathways that can create Floquet states for molecular spectroscopy. Figure 5a shows an

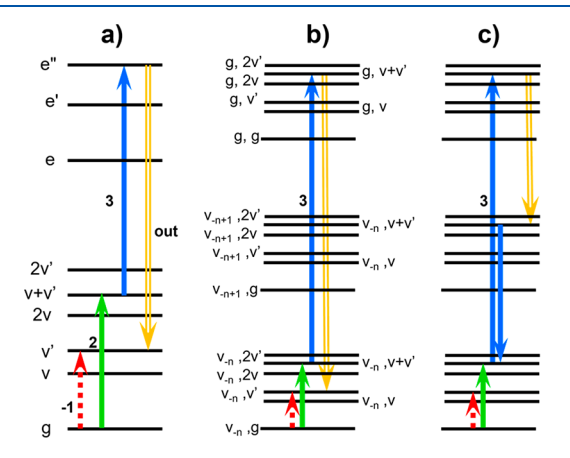


Figure 5. WMEL diagrams: (a) example of the optical and infrared pathway for molecular spectroscopy, (b) example of the molecular non-parametric XUV and infrared pathway, and (c) example of the molecular-stimulated Raman core and optical or infrared pathway.

example of a non-parametric Floquet pathway entangling vibrational fundamentals (v, v'), overtones (2v, 2v'), combination bands (v + v'), electronic states, and vibronic states. Figure 5b shows an example of how a core excitation would add atomic resolution to the Figure 5a pathway. There are many other optical/vibrational Floquet state pathways that are currently used for molecular spectroscopy. ^{2,12,21} In each case, a core excitation could replace the ω_3 optical transition to introduce atomic specificity. Many of these pathways could

also be used for measuring the phonon modes for material applications.

Mukamel proposed using stimulated X-ray Raman as the basis for X-ray CMDS. 5,6 An X-ray Raman excitation involves a core state excitation followed closely by emission from a filled core state that refills the original hole and leaves a hole in an excited valence band. Stimulated X-ray/XUV Raman processes can also create a Floquet state containing optically excited states, including both electronic and/or vibrational states. An example pathway is shown in Figure 5c. The output emission from stimulated X-ray Raman would occur in a different direction and frequency; therefore, with an imaging detector, all of the different output pathways would be observed as individual features in the 2D image. Multidimensional spectra would be obtained by scanning the optical/infrared excitation frequencies while monitoring the intensity of a feature or features. It is expected that features from the pathways in panels b and c of Figure 5 would both appear because a Floquet state remains coherent during the entire time that it is driven and does not display relaxation effects unless there are time delays introduced between pulses.

Although this paper is centered on XUV spectroscopy, it can also form the basis for X-ray Floquet spectroscopy. Experimentally, it is difficult to achieve the long-term phase stability in X-ray free-electron lasers that is required for heterodyning the output signal with the local oscillator used in 2D electronic CMDS because the wavelengths are so short. In Floquet state spectroscopy, the phase relationships between coherences are established in the excitation region within each pulse set; therefore, phase stability between pulse sets is not required. The phase-matched output beams isolate the X-ray coherent component, while any incoherent component is not directional.

The fully coherent nature of Floquet state spectroscopy forms the basis for new applications. Unlike optical pump, Xray/XUV probe methods, a Floquet state remains coherent over the time that it is coherently driven. Because relaxation dynamics destroy the coherence of a Floquet state, the effects of relaxation are not seen in the spectroscopy. Although dephasing still occurs within the Floquet state, the driving fields restore any loss of coherence. As a result, the spectra represent a snapshot of the entangled states at the time of creation. This feature forms the basis for probing the Brillouin zone described earlier. It also forms the basis for a pump-Floquet state probe method that creates a multidimensional spectrum of the dynamics. The multidimensional character of Floquet states can form the basis for an X-ray/XUV microscope with atomic, electronic, and vibrational contrast and atomic-scale spatial resolution. Because the output signals require the presence of all coherences within the Floquet state, the spatial resolution will depend upon the shortest wavelength; for XUV, it is 10 nm. For free-electron lasers, it is even smaller. The atomic spectral selectivity has important applications for chemistry, where Floquet states containing entangled core holes and vibrational modes on the potential energy surface of the reaction can measure the anharmonicity associated with the reaction because the coherent modes play the same role as the incoherent modes that drive reactions. Finally, Floquet state methodology has potential applications for quantum information science. The wave functions within a Floquet state differ from those at equilibrium because the coupling between states provides the engineering required to

manipulate quantum states coherently for quantum control and engineering.

The use of Floquet state spectroscopy has been hampered by the difficulties in scanning excitation frequencies of ultrafast pulses. Experimentally, it is important to maintain temporal overlap and phase matching of the excitation pulses as the optical/infrared frequencies are scanned in order to avoid spectral anomalies. Typically, spectral overlap is maintained by synchronizing pulse delay times to the pulse frequencies. Because phase matching depends upon the refractive index, phase matching must also be maintained by synchronizing the angles between pulses to match the phase matching requirements at the different frequencies. These changes require computer control of the time delays and angles; therefore, synchronization can be maintained over the time required to obtain multidimensional spectra.

ASSOCIATED CONTENT

Supporting Information

The Supporting Information is available free of charge at https://pubs.acs.org/doi/10.1021/acs.jpclett.3c00778.

Derivation of eq 5 from eq 4, table of the parameter values required for estimating the $I_{\rm out}/I_3$ intensity ratio, and discussion of the phase matching required for resolving parametric and non-parametric processes (PDF)

AUTHOR INFORMATION

Corresponding Author

John C. Wright — Department of Chemistry, University of Wisconsin—Madison, Madison, Wisconsin 53706, United States; orcid.org/0000-0002-6926-1837; Email: wright@chem.wisc.edu

Authors

Daniel D. Kohler – Department of Chemistry, University of Wisconsin—Madison, Madison, Wisconsin 53706, United States; orcid.org/0000-0003-4602-2961

Uwe Bergmann – Department of Physics, University of Wisconsin—Madison, Madison, Wisconsin 53706, United States; ◎ orcid.org/0000-0001-5639-166X

Complete contact information is available at: https://pubs.acs.org/10.1021/acs.jpclett.3c00778

Notes

The authors declare no competing financial interest.

ACKNOWLEDGMENTS

This work was supported by the National Science Foundation under Awards CHE-2203290 and CHE-2246379 and the Department of Energy under Award DE-FG02-09ER46664. The authors thank Shaul Mukamel for very helpful discussions.

REFERENCES

- (1) Chu, S.-I.; Telnov, D. A. Beyond the Floquet theorem: Generalized Floquet formalisms and quasienergy methods for atomic and moleculr multiphoton processes in intense laser fields. *Phys. Rep.* **2004**, 390 (1-2), 1-131.
- (2) Wright, J. C.; Chen, P. C.; Hamilton, J. P.; Zilian, A.; LaBuda, M. J. Theoretical Foundations for a New Family of Infrared Four Wave Mixing Spectroscopies. *Appl. Spectrosc.* **1997**, *51*, 949–958.

- (3) Zhao, W.; Wright, J. C. Doubly Vibrationally Enhanced Four Wave Mixing Spectroscopy- The Optical Analogue to 2D NMR. *Phys. Rev. Lett.* **2000**, *84*, 1411–1414.
- (4) Gallagher, S. M.; Albrecht, A. W.; Hybl, J. D.; Landin, B. L.; Rajaram, B.; Jonas, D. M. Heterodyne Detection of the Complete Electric Field of Femtosecond Four-Wave Mixing Signals. *J. Opt. Soc. Am. B* 1998, *15*, 2338–2345.
- (5) Hybl, J. D.; Albrecht, A. W.; Faeder, S. M. G.; Jonas, D. M. Two Dimensional Electronic Spectroscopy. *Chem. Phys. Lett.* **1998**, 297, 307–313.
- (6) Tanaka, S.; Mukamel, S. Coherent X-ray Raman spectroscopy: A nonlinear local probe for electronic excitations. *Phys. Rev. Lett.* **2002**, 89 (4), No. 043001.
- (7) Schweigert, I. V.; Mukamel, S. Coherent ultrafast core-hole correlation spectroscopy: X-ray analogues of multidimensional NMR. *Phys. Rev. Lett.* **2007**, 99 (16), No. 163001.
- (8) Kowalewski, M.; Fingerhut, B. P.; Dorfman, K. E.; Bennett, K.; Mukamel, S. Simulating Coherent Multidimensional Spectroscopy of Nonadiabatic Molecular Processes: From the Infrared to the X-ray Regime. *Chem. Rev.* **2017**, *117* (19), 12165–12226.
- (9) Bencivenga, F.; Capotondi, F.; Foglia, L.; Gessini, A.; Kurdi, G.; Lopez-Quintas, I.; Masciovecchio, C.; Kiskinova, M.; Mincigrucci, R.; Naumenko, D.; Nikolov, I.; Pedersoli, E.; Simoncig, A. Shortwavelength four wave mixing experiments using single and two-color schemes at FERMI. J. Electron Spectrosc. Relat. Phenom. 2022, 257, 146901.
- (10) Jonas, D. M. Two-dimensional femtosecond spectroscopy. *Annu. Rev. Phys. Chem.* **2003**, *54*, 425–463. Khalil, M.; Mukamel, S. Ultrafast spectroscopy and diffraction from XUV to X-ray. *J. Chem. Phys.* **2020**, *153* (10), 100401.
- (11) Attar, A. R.; Chang, H.-T.; Britz, A.; Zhang, X.; Lin, M.-F.; Krishnamoorthy, A.; Linker, T.; Fritz, D.; Neumark, D. M.; Kalia, R. K.; Nakano, A.; Ajayan, P.; Vashishta, P.; Bergmann, U.; Leone, S. R. Simultaneous Observation of Carrier-Specific Redistribution and Coherent Lattice Dynamics in 2H-MoTe₂ with Femtosecond CoreLevel Spectroscopy. *ACS Nano* **2020**, *14*, 15829–15840.
- (12) Lin, Y. C.; Fidler, A. P.; Sandhu, A.; Lucchese, R. R.; McCurdy, C. W.; Leone, S. R.; Neumark, D. M. Coupled nuclear-electronic decay dynamics of O2 inner valence excited states revealed by attosecond XUV wave-mixing spectroscopy. *Faraday Discuss.* **2021**, 228 (0), 537–554.
- (13) Gaynor, J. D.; Fidler, A. P.; Lin, Y.-C.; Chang, H.-T.; Zuerch, M.; Neumark, D. M.; Leone, S. R. Solid state core-exciton dynamics in NaCl observed by tabletop attosecond four-wave mixing spectroscopy. *Phys. Rev. B* **2021**, *103* (24), 245140. Marroux, H. J. B.; Fidler, A. P.; Neumark, D. M.; Leone, S. R. Multidimensional spectroscopy with attosecond extreme ultraviolet and shaped near-infrared pulses. *Sci. Adv.* **2018**, *4*, eaau3783.
- (14) Wright, J. C. Analytical chemistry, multidimensional spectral signatures, and the future of coherent multidimensional spectroscopy. *Chem. Phys. Lett.* **2016**, *662*, 1–13.
- (15) Wright, J. C. Multiresonant Coherent Multidimensional Spectroscopy. *Annu. Rev. Phys. Chem.* **2011**, *62*, 209–230.
- (16) Wright, J. C. Coherent Multidimensional Vibrational Spectroscopy. *Int. Rev. Phys. Chem.* **2002**, *21*, 185–255.
- (17) Brisk, M. A.; Baker, A. D. Shake-up Satellites in X-ray Photoelectron-Spectroscopy. *J. Electron Spectrosc. Relat. Phenom.* **1975**, 7 (3), 197–213.
- (18) Wright, J. C.; Carlson, R. J.; Hurst, G. B.; Steehler, J. K.; Riebe, M. T.; Price, B. B.; Nguyen, D. C.; Lee, S. H. Molecular, Multiresonant Coherent Four Wave Mixing Spectroscopy. *Int. Rev. Phys. Chem.* **1991**, *10*, 349–390.
- (19) Steehler, J. K.; Wright, J. C. Parametric and Non-parametric Four Wave Mixing in Pentacene:p-Terphenyl. *J. Chem. Phys.* **1985**, 83, 3200–3208.
- (20) Carlson, R. J.; Wright, J. C. Line Narrowing in Multiresonant Third Order Molecular Spectroscopies. *J. Mol. Spectrosc.* **1990**, *143*, 1–17.

- (21) Breidbach, J.; Cederbaum, L. S. Universal attosecond response to the removal of an electron. *Phys. Rev. Lett.* **2005**, *94* (3), 033901.
- (22) Kwak, K.; Cha, S.; Cho, M. H.; Wright, J. C. Vibrational interactions of acetonitrile: Doubly vibrationally resonant IR-IR-visible four-wave-mixing spectroscopy. *J. Chem. Phys.* **2002**, *117* (12), 5675–5687.
- (23) Wright, J. C. Applications of the New Family of Coherent Multidimensional Spectroscopies for Analytical Chemistry. *Annu. Rev. Anal. Chem.* **2017**, *10*, 45–70.
- (24) Wright, J. C. Fully Coherent Schrodinger Cat State Spectroscopy and the Future of CMDS. In *Coherent Multidimensional Spectroscopy*, 1st ed.; Cho, M., Ed.; Springer Nature: Singapore, 2019; Springer Series in Optical Sciences, Vol. 226, pp 145–170, DOI: 10.1007/978-981-13-9753-0_7.